Dynamic coupling of rigid in-plane pore oscillations and flow through nanoporous two-dimensional membranes

J. P. Martínez Cordeiro and N. R. Aluru*

Walker Department of Mechanical Engineering, Oden Institute for Computational Engineering and Sciences, The University of Texas at Austin, Austin, Texas 78712, USA

(Received 16 December 2023; accepted 25 April 2024; published 3 June 2024)

Most of the literature on flow through nanoporous two-dimensional membranes has focused on static membranes under quasiequilibrium conditions. However, various studies have shown the relevance of fluid-structure interactions—particularly dynamic coupling—on flow through nanopores and nanotubes. A fundamental understanding of the effects of membrane oscillations could provide the missing link to the development of ultraefficient nanofluidic systems for water desalination, gas separation, and other applications. Herein, we use molecular dynamics simulations to study the effects of rigid in-plane harmonic pore oscillations on water flow through nanoporous graphene. First, we repurpose a used technique as a framework to avoid injecting arbitrary amounts of heat into the interfacial water, thereby isolating the physical mechanisms caused by the pore's movement. Then we demonstrate that the considered pore oscillations enhance flow by increasing the average axial velocity and decreasing the average density of water inside the pore due to the dynamic opening and closing of flow routes inside the pore. Finally, we show how these effects manifest themselves in relevant fluid properties for both single-file or collective-diffusion and frictional flows.

DOI: 10.1103/PhysRevFluids.9.064201

I. INTRODUCTION

Since in classical hydrodynamics water flux scales inversely with membrane thickness [1–5], two-dimensional (2D) membranes have become promising prospects for novel highly efficient nanofluidic systems for water desalination [6,7], nanopower generation [8], biological sensing [9–12], etc. In fact, ultrathin nanoporous membranes (such as single-layer graphene) display water transport rates that are orders of magnitude larger than expected from the classical models [7,13–17]. Traditional models describing flows through pores at different levels of accuracy (e.g., the Hagen-Poiseuille (HP) model for flows through long pipes [1,2], the Sampson model for flows through zero-thickness pores [3], and the Dagan model for flows through finite-thickness pores [4]) fail to consider the presence of slip and viscosity variations at the pore interface [5,16,18,19]. As 2D nanopores became an experimental reality, new models emerged as corrections to the classical ones, providing a better understanding of flow through 2D nanopores (e.g., Suk and Aluru's corrected HP model for flow through graphene pores [16], Gravelle *et al.*'s corrected Sampson model for flow through hourglass aquaporins [20], and Heiranian *et al.*'s corrected Sampson-Dagan model for flow through graphene pores [5]). Even though the mysteries of flow enhancement through membranes approaching the limit of atomic thinness have been largely unraveled, most of the effort has focused on static membranes under equilibrium or quasiequilibrium conditions. This is particularly puzzling because some of the most efficient and fascinating biological systems

*Corresponding author: aluru@utexas.edu

contain dynamic porous membranes and channels [21,22]. Potential solutions to the gargantuan problems facing modern society, such as the worldwide water shortage [23–27], could come from advances in dynamic nanofluidics. Yet, to optimize and fine-tune nanoengineering systems that fully exploit the advantages displayed in their biological counterparts, it is necessary to gain a profound understanding of the effects of dynamic nanoporous membranes on flow as well as the physical mechanisms underlying them.

Several authors have considered the effects of dynamic substrates on flow at the nanoscale, with great emphasis on dynamic carbon nanotubes (CNTs) [28–38]. Other numerical and analytical papers have also studied the effects of oscillatory substrates, even showing the ability to tune flow properties through particular sorts of actuation [39–42]. Recently, the attention has turned to dynamic 2D ultrathin nanoporous membranes. Noh and Aluru examined the effects of thermal fluctuations and driving-force-induced membrane deformations on pressure-driven flow [43]. They determined that a large component of the flux comes from phonon-fluid coupling. In that study, they modeled thermal fluctuations as rigid out-of-plane membrane oscillations that satisfy the constraint $\langle \mathrm{KE}_{\mathrm{imposed}} \rangle = \mathrm{TE}(T_{\mathrm{sys}})$, where $\langle \mathrm{KE}_{\mathrm{imposed}} \rangle$ is the time-averaged kinetic energy that is being synthetically imposed on the membrane, and $\mathrm{TE}(T_{\mathrm{sys}})$ is the thermal energy that the membrane would have if it were thermalized at system temperature, T_{sys}. This was done because the imposed oscillations were not supposed to model externally applied oscillations, but rather intrinsic thermal fluctuations that result from the mere fact that the membrane is at a particular temperature. This type of oscillation was then analyzed in a subsequent work that considered the effects of substrate oscillations—subject to the same constraint—on interfacial fluid, particularly the effects on wettability and nanoporous flow [44]. It was found for water flow that oscillations at the bending frequency of water increase the hydrophobicity of the substrate and reduce the wall-fluid friction, enhancing flow through 2D nanoporous membranes. Similar studies were carried out for voltage-driven flows of electrolytic solutions [45]. Most recently, Li *et al.* performed a study considering rigid in-plane oscillations—although not subject to the thermal energy constraint—for the application of water desalination using a covalent organic framework (COF) membrane, a particular type of 2D membrane with high flexibility and high porosity [46]. They discovered that the membrane oscillations enhance flux while maintaining high selectivity due to what they called "spatial permeability": the reduction of hydrogen bonds per water molecule up to 15 Å away from the membrane as a result of collisions with the pore walls. They found that flux increases with increasing amplitude and/or decreasing frequency. However, they did not report relationships between the amplitude or frequency and the flow enhancement—possibly since their oscillation scheme artificially injects arbitrary amounts of energy into the system at the interface. By not subjecting their oscillations to the thermal energy constraint, the effects of the dynamic pores become indistinguishable from those of heat transfer from the membrane to the interfacial water. Furthermore, by first considering a COF for water desalination in addition to their choice of oscillation scheme, the study fails to unravel the fundamental physical mechanisms behind the observed phenomena. Through this study, we bridge that gap in the fundamental understanding of the effects of in-plane rigid pore oscillations on flow.

We used molecular dynamics (MD) simulations of pressure-driven water flow through a nanoporous single-layer graphene membrane subject to rigid in-plane oscillations. To isolate the effects of the dynamic pore, we maintain the imposed kinetic energy of the membrane equal to the thermal energy it would have at the system's temperature. We find flow enhancement relative to the static case for all cases considered for frequencies $f_{\mathrm{osc}} \in [0, 100]$ cm^{-1} and pressure drops $\Delta p \in [50, 300]$ MPa. The degree of enhancement was determined by the relative competition between an increasing average axial velocity and a decreasing average water density inside the pore for increasing amplitudes (decreasing frequencies). By analyzing the transient profiles inside the pore, we discovered that the physical mechanism underlying the observed phenomena is related to the opening and closing of flow routes inside the dynamic pore. The amplitude controls the number of routes that are opened or closed, and the frequency determines the speed at which these routes open or close. Finally, we show how these effects manifest themselves in the relevant flow

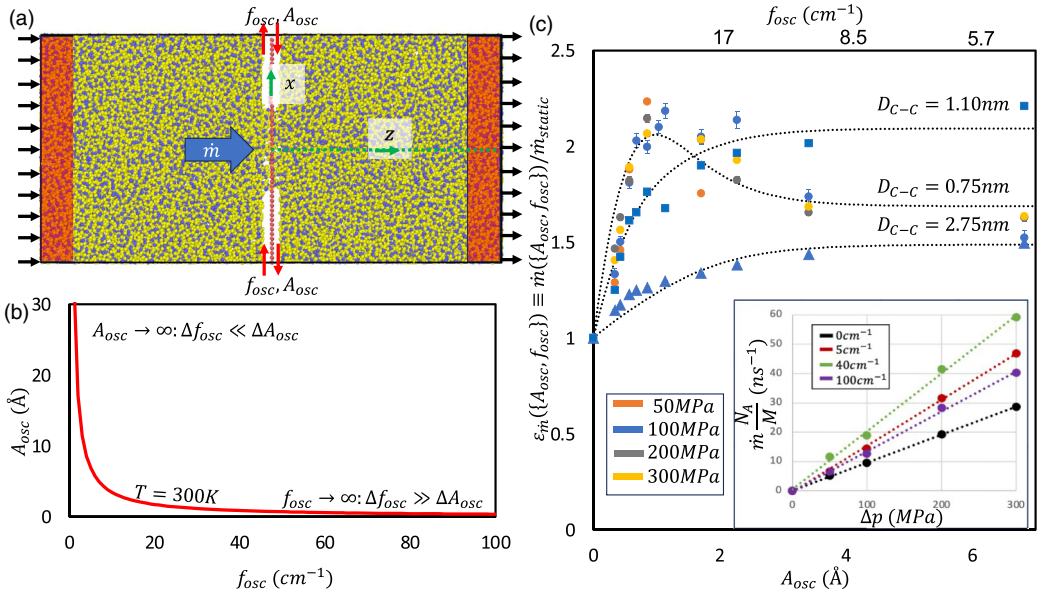

FIG. 1. System, oscillation scheme, and flux enhancement results. (a) Visual representation of MD simulation system for pressure-driven flow through a graphene nanopore undergoing in-plane oscillations. The pore geometries are shown in Fig. S1 of the Supplemental Material [48]. (b) Set of amplitudes and frequencies corresponding to $T = 300$ K under our oscillation scheme. (c) Flux enhancement factors for $\Delta p = [50,\ 100,\ 200,\ 300]$ MPa and $D = [0.75,\ 1.1,\ 2.75]$ nm at $f_{\rm osc} \in [0, 100]\,{\rm cm}^{-1}$. Dashed lines are the functional relationships fit to the data. Enhancement is observed for all cases, and enhancement factors decrease with increasing pore size. The inset shows the linear increase of molecule flow rate with increasing pressure for various frequencies and $D = 0.75$ nm.

properties for both single-file or collective-diffusion and frictional flows. This study provides the desired fundamental understanding that will lead to the design and optimization of finely tuned ultraefficient nanofluidic transport systems which might prove technologically important in the coming years.

II. METHODS

We performed nonequilibrium molecular dynamics (NEMD) simulations of pressure-driven water flow through graphene nanopores using LAMMPS [47]. A schematic of one of the systems considered is shown in Fig. 1(a). The geometries of the pores used are shown in Fig. S1 of the Supplemental Material [48]. The simulation was performed in the canonical ensemble (*NVT*) with a time step of 1 fs and a Nosé-Hoover chains thermostat [49] maintained the temperature at 300 K with three thermostat chains and a damping parameter of 100 time steps. Once the pressure drop was introduced, the thermostat was only applied in the x and y directions to not affect the dynamics in the direction of transport. Periodic boundary conditions (PBCs) were applied in all directions. The membrane was placed in the x-y plane with the armchair configuration in the x direction and the zigzag configuration in the y direction. The pore was placed in the center of the membrane. We considered pores with center-to-center diameters (the average distance between the centers of diametrically opposed pore-lining atoms) of 0.75, 1.10, and 2.75 nm. For the 0.75- and 1.10-nm pores, $L_x = 38.34$ Å and $L_y = 39.3522$ Å, while for the 2.75-nm pore, $L_x = 59.64$ Å and $L_y = 59.0283$ Å. The Lennard-Jones (LJ) potential was used to model the van der Waals interactions with a cutoff distance of 1.2 nm. The LJ potential parameters for the graphene-water

interactions used are the ones developed by Wu and Aluru [50]. Long-range Coulomb interactions were calculated with the particle-particle particle-mesh (PPPM) method [51] with an accuracy of 10^{-5}. To rigidly oscillate the membrane, which requires imposing a harmonically oscillating trajectory to all membrane atoms, we maintained a rigid membrane throughout the simulation by not integrating the positions of the membrane's atoms. By making the membrane rigid, the membrane fluctuations are neglected.

Two water reservoirs spanning the area of the membrane and extending 60 Å in the direction of transport (z direction) were positioned on each side of the porous membrane. The water was modeled using the single point charge extended (SPC/E) water model [52]. It has been reported that flexible water models have minimal effects on the dynamics of water through graphene pores [7]. The water bonds and angles were fixed by using the SHAKE algorithm [53].

Each simulation was run with three to six different initial configurations (different initial positions and initial velocities) so that we could better sample the phase space. After equilibrating the system in the *NVT* ensemble as described above and confirming that the density of water within the furthest 10 Å from the membrane remained close to the bulk density of water at 300 K, we ramped up the applied pressure drop to the desired value and rigidly and harmonically oscillated the membrane in the x direction. We considered pressure drops of 50, 100, 200, and 300 MPa. Although various methods for applying pressure drops in MD simulations exist [54,55], we applied an external force $f = \Delta pA/n$ (where Δp is the applied pressure drop, A is the area of the membrane, and n is the number of particles in the region where the external forces are applied) on each water molecule's oxygen atom when they are inside of a designated region. In our case, there were two regions of identical dimensions spanning the entire x-y cross-section area of the simulation box and 10 Å located at the ends of the simulation box in the z direction. This method has been used by several authors [56–59], including studies with dynamic membranes. The membrane was oscillated rigidly by imposing that all its atoms follow the trajectory given by $x(t) = x_0 + A_{\text{osc}} \sin(2\pi f_{\text{osc}} t)$, where x_0 is each atom's initial x coordinate, A_{osc} is the oscillation amplitude, and f_{osc} is the oscillation frequency. In order to supply a constant average amount of energy to the system through the membrane oscillations—for reasons argued in Sec. III—the frequencies and amplitudes were constrained such that $A_{\text{osc}} = \frac{1}{2\pi f_{\text{osc}}}\sqrt{\frac{2k_B T_{\text{sys}}}{M}}$, where k_B is Boltzmann's constant, T_{sys} is the temperature of the thermostat, and M is the molar mass of carbon. We considered frequencies of $0-100\,\text{cm}^{-1}$, each with its corresponding amplitude value. These frequencies are approximately in the range of frequencies that other studies demonstrating flow enhancement in nanopores and nanotubes have shown to maximize the benefits of dynamic substrates. To make sure that nothing unexpected was occurring at the edges of the box between periodic images, we ran simulations without nanopores and confirmed that the flux in the direction of the pressure drop was exactly null. After 200 ps of ramping the pressure drop, the system was allowed to stabilize for another 200 ps. Then production runs were run for 5–20 ns.

III. OSCILLATORY SCHEME

As mentioned before, substrate oscillations in nanofluidic systems have been considered before. A potential issue with these studies is that, since different combinations of amplitudes and frequencies introduce different amounts of average kinetic energy into the system, they are unable to separate the effects of the dynamic structure from the effects of injecting an arbitrary amount of energy into the system. This is problematic if the aim of the studies is to gain a fundamental understanding of the dynamic fluid-structure coupling. Since such an understanding of the effects of the oscillations and the physical mechanisms underlying them is essential in the pursuit of fine-tuned, optimized, and even controllable nanofluidic devices, it is crucial to isolate the effects of the oscillatory structure on the flow. Noh and Aluru introduced the thermal energy constraint on the oscillations they considered originally as a simplified way of analyzing the effects of intrinsic thermal fluctuations [43–45,60]. The thermal energy constraint sets the average kinetic energy of

the substrate equal to the thermal energy it would have if it were thermalized, i.e.,

$$\langle \mathrm{KE}_{\mathrm{imposed}} \rangle = \mathrm{TE}(T_{\mathrm{sys}}). \tag{1}$$

Since the imposed motion is harmonic,

$$x(t) = x_0 + A_{\mathrm{osc}} \sin(2\pi f_{\mathrm{osc}} t), \tag{2}$$

and

$$v(t) = 2\pi f_{\mathrm{osc}} A_{\mathrm{osc}} \cos(2\pi f_{\mathrm{osc}} t). \tag{3}$$

This implies that the average imposed kinetic energy of N atoms is given by

$$\langle \mathrm{KE}_{\mathrm{imposed}} \rangle = f_{\mathrm{osc}} \int_0^{1/f_{\mathrm{osc}}} \sum_{i=1}^{N} \frac{1}{2} m_i v_i^2(t) dt. \tag{4}$$

Since the motion of the membrane atoms is restrained to be only along the x direction, the thermal energy that a membrane with N atoms would have at system temperature would be

$$\mathrm{TE}(T_{\mathrm{sys}}) = \frac{N k_b T_{\mathrm{sys}}}{2}. \tag{5}$$

Carrying out the integrals in Eq. (4) and setting equal to Eq. (5), we get the relationship for our oscillation scheme between the amplitude and frequency:

$$A_{\mathrm{osc}} = \frac{1}{2\pi f_{\mathrm{osc}}} \sqrt{\frac{2 k_B T_{\mathrm{sys}}}{M}}. \tag{6}$$

This implies that each amplitude corresponds to exactly one frequency, and that amplitude and frequency are inversely related. For graphene at $T_{\mathrm{sys}} = 300$ K, the allowed sets of amplitudes and frequencies—referred to as oscillatory states in this work—are shown in Fig. 1(b). Despite the coupling between amplitude and frequency that is inherent for this oscillatory scheme, Noh and Aluru were able to use it to show the frequency effects of the dynamic coupling between an out-of-plane oscillating nanoporous membrane and the fluid in which it is immersed [43–45,60]. However, the complete separation of amplitude and frequency effects is not guaranteed for all kinds of substrate actuation.

It must be emphasized that in this work we employ this scheme not because of an interest in modeling intrinsic thermal fluctuations, but rather as a means of considering the dynamic effects of the oscillatory pore on flow through it without injecting an arbitrary amount of energy into the system at the interface. This choice might seem strange at first because experimentally the arbitrary injection of energy is not a concern, as the heat would dissipate naturally, leading to insignificant changes in temperature. However, in computational simulations, due to the difference in length and timescales involved, arbitrary choices of amplitudes and frequencies do not necessarily allow for proper temperature control. This is problematic for reproducing the canonical ensemble, as well as for not departing significantly from equilibrium—since local differences in temperature are a measure of departures from equilibrium [61]—which is desirable for analytical purposes. While experimentalists might not encounter similar difficulties, our oscillatory scheme in experiments should allow for negligible amounts of heat dissipation. Finally, it should be noted that studying systems with negligible heat dissipation is of interest because it provides a more fundamental understanding of the physical mechanisms related to the effects of dynamic substrates.

IV. RESULTS AND DISCUSSION

To observe the effects of an oscillatory pore on flow through it, we calculate the flux for different pressures, pore diameters, and oscillatory states by computing the slope of the running average net

number of molecules that cross the pore in the direction of the pressure drop. The mass flow rate, $\dot{m}$, computed for the 0.75- and 2.75-nm pores, agrees well with published results [18]. To compare the flow rates at different oscillatory states with the flow rates for the static membranes, we make use of an enhancement factor defined as

$$\varepsilon_\alpha(\{A_{\mathrm{osc}}, f_{\mathrm{osc}}\}) \equiv \frac{\alpha(\{A_{\mathrm{osc}}, f_{\mathrm{osc}}\})}{\alpha_{\mathrm{static}}}, \tag{7}$$

where α is the quantity of interest, in this case the flux. For a given oscillatory state, $\varepsilon > 1$ signifies an increase relative to the static case. The flux enhancement factors for all the cases considered appear as a function of amplitude in Fig. 1(c). We found an increase in flux for all oscillatory states, and that the degree of enhancement increases with decreasing pore diameter, which implies that the observed improvement in flux is related to the physical interactions occurring at the pore wall interface.

For the stationary pore, we expect $\dot{m}$ to show a linear dependence on Δp since the Reynolds number throughout our studies is in the Stokes or creeping flow range (Re $\ll 1$). As evident in the inset of Fig. 1(c), this linearity is maintained for all the oscillatory states considered. From classical hydrodynamics,

$$\dot{m} = v\rho A, \tag{8}$$

where v is the fluid's average axial velocity, ρ is the average fluid density inside the pore, and A is the cross-section area of the pore. To decompose the observed effects on flow, we analyzed how each of these quantities changed for different oscillatory states. By looking at the velocity and molecule number density profiles relative to the center of the pore at each instant in time in Fig. 2(a), three general trends are clear: an increase in amplitude (decrease in frequency) causes (i) an increase in the velocity, (ii) a decrease in the average water density inside the pore, and (iii) no change in the pore area. It should be noted that for all oscillatory states the water tends to increasingly lose its structure near the walls with increasing amplitude (decreasing frequency), and that the velocity profiles are still parabolic as expected in classical hydrodynamics for stationary pores. We compute velocity and density enhancement factors—shown in Figs. 2(c) and 2(d), respectively—to compare the effects on velocity and density for different oscillatory states. The enhancement factors for the average axial velocity and average pore density increase and decrease, respectively, until both reach a saturation point at a high enough amplitude (low enough frequency). The dashed lines in the plot are sigmoid curves that were fit to the data. The average axial velocities are proportional to the pressure drop, and the density is pressure invariant. In fact, the densities for the various oscillatory states were constant even in the case of no pressure drop. Since the decomposed trends for the axial velocities and densities are indeed similar across all nanopores, we suppose that the underlying physical mechanism is the same for all nanopores, and we focus our analysis on the largest pore (the 2.75-nm pore) due to improved statistics.

To understand the physical mechanism underlying these effects, we computed the time-averaged velocity and molecule number density profiles in the radial direction relative to the initial position of the pore center. The profiles for various oscillatory states corresponding to low, medium, and high amplitudes are shown in Fig. 2(b). The molecule number density profile relative to the initial position of the pore center demonstrates that, as the amplitude of oscillation increases, water is allowed to flow through regions that used to be impermeable. Even though the water-accessible pore area at any instant is constant, the oscillation of the pore changes the flow routes or lanes (as an analog to traffic flow) that water is able to use in its path past the membrane. Furthermore, the velocity profile shows that the water molecules in these new routes have surprisingly high velocities in comparison to the retardation that entropy barriers cause for pure diffusion [62], as discussed in the Supplemental Material [48]. These results lead us to believe that the observed phenomena for flows through oscillating pores can be explained by the dynamic opening and closing of flow routes.

Interestingly, even for very low amplitudes, the velocity profile undergoes points of inflection ($du/dr = 0$). Even though the profiles relative to the center of the pore at each instant in time

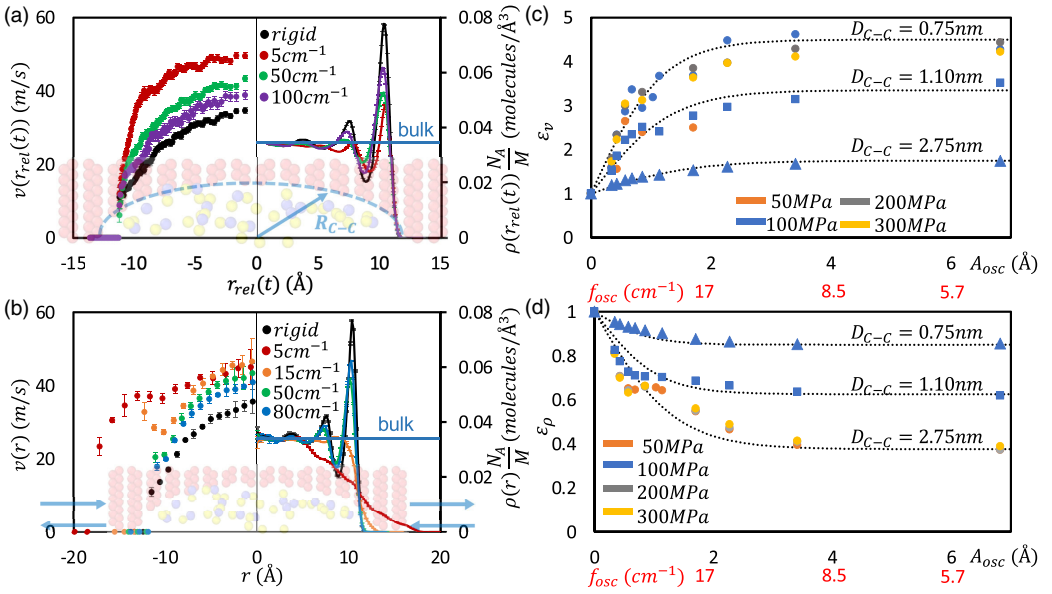

FIG. 2. Average axial velocity, average pore molecule number density, and pore size results. (a) Radial axial velocity (left), and radial molecule number density (right) time-averaged profiles relative to the pore center at each instant for $D = 2.75$ nm, $\Delta p = 100$ MPa, and multiple frequencies. Note that the x axis of the plot shows the position relative to the center of the pore at each instant, $r_{\mathrm{rel}}(t) = \sqrt{(x(t) - x_{\mathrm{pc}}(t))^2 + (y(t) - y_{\mathrm{pc}}(t))^2 + (z(t) - z_{\mathrm{pc}}(t))^2}$, where $x(t)$, $y(t)$, $z(t)$ are the coordinates at time t relative to the initial pore center (the origin), and $x_{\mathrm{pc}}(t)$, $y_{\mathrm{pc}}(t)$, $z_{\mathrm{pc}}(t)$ are the coordinates of the pore center at time t relative to the origin. The density profile shows that the density falls below 2% bulk density at the same radial distance from the center of the pore at each time step. (b) Radial axial velocity (left), and radial molecule number density (right) time-averaged profiles relative to the original pore center for $D = 2.75$ nm, $\Delta p = 100$ MPa, and multiple frequencies. (c) Average axial velocity enhancement factors for $\Delta p = [50,\ 100,\ 200,\ 300]$ MPa and $D = [0.75,\ 1.1,\ 2.75]$ nm at $f_{\mathrm{osc}} \in [0, 100]\,\mathrm{cm}^{-1}$. Dashed lines are the functional relationships fit to the data. Average axial velocity is monotonically increasing for increasing amplitude. The average axial velocities for the static pores at 100 MPa were 2.25 m/s for the 0.75-nm pore, 4.70 m/s for the 1.10-nm pore, and 22.5 m/s for the 2.75-nm pore. (d) Average pore density enhancement factors for $\Delta p = [50,\ 100,\ 200,\ 300]$ MPa and $D = [0.75,\ 1.1,\ 2.75]$ nm at $f_{\mathrm{osc}} \in [0, 100]\,\mathrm{cm}^{-1}$. Dashed lines are the functional relationships fit to the data. Average pore density decreases with increasing amplitude. The average numbers of molecules inside the static pore at each time step were 1.4 for the 0.75-nm pore, 3.9 for the 1.10-nm pore, and 50.7 for the 2.75-nm pore.

seem to maintain the applicability of continuum models, the steady-state profiles exhibit behavioral deviations from continuum hydrodynamics that increase with increasing amplitude. Also, from the molecule number density profile it can be seen that, as the amplitude increases, the water's structure is weakened to the point that for high enough amplitudes it is nearly destroyed. A similar result was demonstrated by Noh and Aluru for flow through a nanochannel with the walls of the nanochannel oscillating in the out-of-plane direction synchronously; however, in that case the density was least structured at the bending frequency of water ($\sim$50 cm^{-1}) [44].

Since the trends in density and velocity—and, thus, in flux—at different oscillatory states seemed to arise from the dynamic opening and closing of flow routes, we calculated the transient molecule number density and velocity. A video showing these transient profiles through a period of oscillation can be found in Supplemental Video 1 [48], and Fig. 3 shows snapshots of these transient profiles at the instants of highest pore velocity ($t^* \equiv 2\pi f_{\mathrm{osc}} t = n\pi,\ \forall\, n \in \mathbb{Z}$) and highest pore displacement ($t^* = n\pi/2,\ \forall\, n \in \mathbb{Z}$). These illustrations make evident that, as the pore oscillates, it opens new

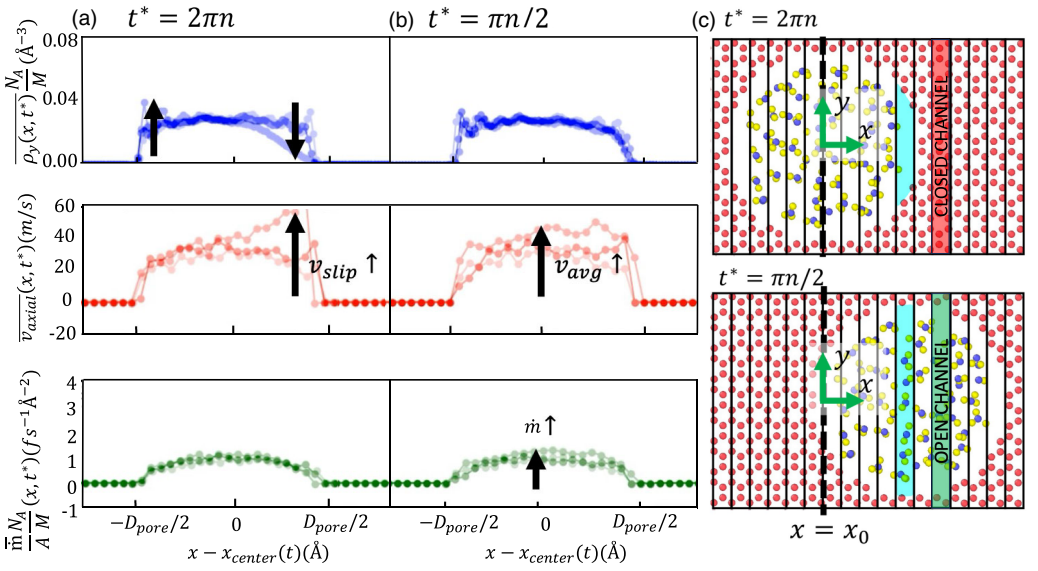

FIG. 3. Superimposed transient molecule number density, axial velocity, and molecule flow rate per unit area profiles with respect to x (x direction is the direction parallel to direction of oscillation) averaged over the y direction for $D = 2.75$ nm, $\Delta p = 100$ MPa at different times in the period of oscillation for low, medium, and high frequencies. The big black arrows show the observed trends that followed an increase in amplitude. (a) Transient profiles at time of maximum pore velocity. As amplitude increases, the density near the departing wall at the new flow routes suffers the destruction of structure. A high slip velocity arises in the new flow routes. (b) Transient profiles at time of maximum pore displacement. As amplitude increases, the high slip velocity in the new flow routes diffuse through the pore, resulting in an increase in average axial velocity. (c) Representation of binning for the calculation of these profiles. This pictorial representation is not produced to scale. At each time, the number of molecules in each bin is normalized by the transient area of the pore in each bin (the area shaded in blue in the diagram).

flow routes while closing existing ones. As the pore closes routes, the water molecules in the center of the pore feel the van der Waals repulsion from the approaching pore wall, which is apparent from the presence of water layering near the wall closing flow routes. Newly open routes, on the other hand, fill up rather slowly and the water in them lacks the layering structure due to the diminishing van der Waals repulsion from the departing pore wall. For the fluid and oscillatory scheme considered in this work, the closing of flow routes (determined by the velocity of the pore, that is, by the oscillatory scheme) occurs more quickly than the filling of new routes (dependent on both the velocity of the pore and the viscosity of the fluid). Since the amplitude controls the number of flow routes that are opened and closed, a higher amplitude would lead to the observed lower density. Furthermore, the newly opened routes exhibit surprisingly high sliplike velocities which diffuse through the rest of the fluid in the pore as the pore slows down and reaches the point of maximum pore displacement, resulting in higher velocities for increasing amplitudes. While the amplitude determines the number of flow routes that open and close, the frequency determines how quickly the opening and closing of routes occurs. Since the mechanism depends on the velocity of the pore relative to the viscosity of the fluid, choosing a slower pore velocity or a less viscous fluid might lead to quicker filling of recently open routes, thus diminishing the effects of this mechanism. For opposite reasons, a quicker pore velocity or a more viscous fluid might further highlight the effects of this mechanism.

The underlying physical mechanisms governing flow through oscillating pores—the dynamic opening and closing of flow routes together with the spatial permeability mechanism (the breaking

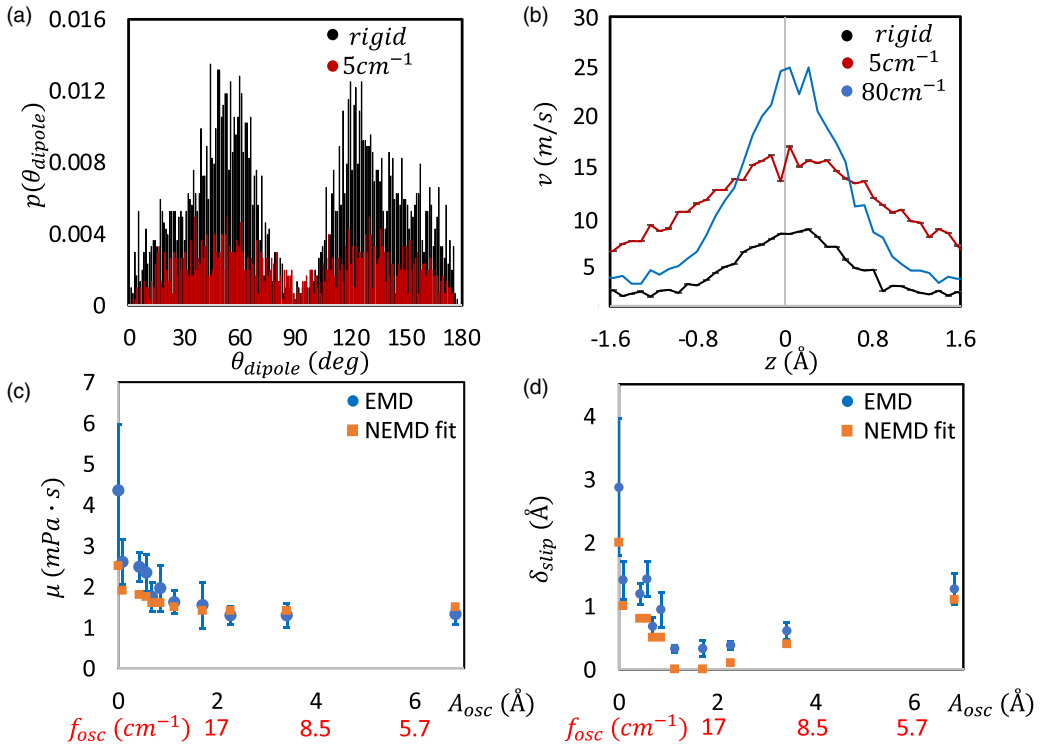

FIG. 4. Effects on single-file or collective-diffusion and frictional flow properties. (a) Probability distribution function of dipole orientation for static case and high-amplitude case normalized with the density of the static case for the 0.75-nm pore. The number of defects (dipole orientation of 90°) remains relatively constant, meaning even though there are less water molecules, they tend to have fewer hydrogen bonds per molecule. (b) Velocity profile for single-file flow in the direction of transport for the 0.75-nm pore. The molecules go through the pore more quickly, so the presence of defects does not slow down the flow relative to the static case. (c) Viscosity values found through the GK formalism (blue dots) compared with viscosities from slip-corrected HP fits (orange squares) for the 2.75-nm pore. As amplitude increases (frequency decreases), the viscosity decreases. (d) Slip lengths found from NEMD profiles and EMD viscosities for the 2.75-nm pore.

of hydrogen bonds due to collisions with the pore walls)—manifest themselves in other properties that are relevant to flow through 2D nanopores. Previous studies have shown that water flow through graphene nanopores is either single-file flow and/or collective diffusion (in smaller pores) or frictional (in larger pores) flow [18]. In single-file flow, the water molecules form a water wire that travels through the pores. A characteristic property of single-file flow through 2D membranes is the presence of defects (dipole orientations of 90° with respect to the z axis) in the water wire: these correspond to breaking and forming of hydrogen bonds as the water molecules reorient themselves [18]. These defects partly explain why single-file flow through 2D membranes is slower than through CNTs [18]. The probability distribution functions of the dipole orientation of water molecules inside the 0.75-nm pore—normalized by average density inside the static pore—for the static and high-amplitude oscillatory cases appear in Fig. 4(a). Since the probability distribution functions were normalized by the average density inside the static pore, the absolute number of defects for each case is visually observable. Interestingly, the number of defects is nearly identical in both the static and oscillatory cases; however, the water flow speeds up, as can be seen in Fig. 4(b). The presence of approximately the same number of defects despite the decrease in pore density is in line with the reduction of hydrogen bonds per molecule reported by Li *et al.* [46]. For larger

pores the flow is primarily frictional, and the velocity profiles have been shown to be qualitatively approximated by Suk and Aluru's corrected HP equation [16]:

$$u(r) = \left(-\frac{1}{4\mu}r^2 + \frac{R^2}{4\mu} + \frac{R}{2\mu}\delta\right)\frac{\Delta p}{L_h}, \tag{9}$$

where μ is the fluid viscosity, R is the pore radius, δ is the slip length, Δp is the pressure drop, and L_h is the hydrodynamic membrane length. In this work, we use the hydrodynamic length computed by Suk and Aluru for the 2.75-nm pore [16], as it allows for their corrected HP equation to implicitly account for variations in viscosity as well as the expected strong entrance and exit effects. We calculated the water viscosity inside the pore using the Green-Kubo (GK) formalism [63]:

$$\mu_{\alpha\beta} = \frac{V}{k_B T}\int_0^\infty \langle P_{\alpha\beta}(0)\cdot P_{\alpha\beta}(t)\rangle dt, \tag{10}$$

where V is the water-accessible pore volume, k_B is Boltzmann's constant, T is the temperature of the system, and $P_{\alpha\beta}(t)$ are the relevant shear components of the stress tensor. In this case, since transport is in the z direction, we use $\mu = \frac{\mu_{xz}+\mu_{yz}}{2}$. Even though the slip length could also be found using a GK relation, it can be computed using the slip velocities measured in the NEMD profiles and the equilibrium molecular dynamics (EMD) GK viscosities through the relation

$$\delta = \frac{\mu U_{\text{slip}}}{\tau_{\text{interface}}}, \tag{11}$$

where U_{slip} is the slip velocity from the time-averaged profiles relative to the pore center [the profiles shown in Fig. 2(a)], and $\tau_{\text{interface}}$ is the friction force per unit pore area. The NEMD approach to calculating the slip length has been used in other works to minimize the high error bars from the GK relations [19]. Since GK relations are obtained using linear response theory, care should be exercised when they are used for nonequilibrium situations. However, as seen in Figs. 4(c) and 4(d), the EMD viscosities and slip lengths agree well with the NEMD values computed by fitting Suk and Aluru's corrected HP velocity to the NEMD profiles (both the GK cumulative integrals and the NEMD fits appear in the Supplemental Material, Figs. S2 and S3 [48]). This shows that Suk and Aluru's corrected HP model still gives good estimates for the behavior of flow through large nanopores under in-plane oscillations, particularly for small amplitudes (high frequencies), even though the model fits worsen for larger amplitudes as the effects due to the sinusoidal perturbation become more nonlinear. Furthermore, the decrease in viscosity due to oscillations contributes to flow enhancement implicitly through the decrease of hydrogen bonds per water molecule shown by Li *et al.* [46], as it is known that the viscosity of water depends on the number of intermolecular hydrogen bonds [64,65].

While our results show trends that agree with what was published by Li *et al.* [46], there are key differences in the studies that justify the differences in the observed effects. Our highest flux enhancement factors are lower than theirs. This could be due to the arbitrary injection of energy at the interface that arises from not subjecting the prescribed oscillations to the thermal energy constraint that we used. It could also be due to the ultrahigh porosity of their COF membrane. Since their membrane is much more porous, they are more likely to observe the effects of spatial permeability—as there are more pores per membrane area, there are more walls and thus more collisions. However, they are less likely to observe the dynamic opening and closing of flow routes that we observed: the opening of their flow routes from the dynamic walls might open more quickly since the water molecules that are new to a given pore were already in the presence of another pore; thus they were more susceptible to transport already. Finally, we should point out that since the dynamic opening and closing of routes is related to the coupling of timescales between the fluid's motion and the pore velocity, different trends might be observed for fluids with vastly different bulk viscosities or for higher or lower "pore temperatures" (leading to a different set of oscillatory states that move the pore at a higher or lower average velocity). These questions are left for further investigation.

V. CONCLUSION

In this study, we performed MD simulations of pressure-driven water flow through a rigid nanoporous single-layer graphene membrane rigidly oscillating in plane in such a way that the effects of the dynamic pore can be isolated. We showed that the flux was enhanced for all oscillatory states considered, and that this enhancement was due to the interplay of increasing velocities and decreasing densities inside the pore as the amplitude of oscillation increases. These phenomena, in turn, were the result of the dynamic opening and closing of flow routes by the oscillating pore. Finally, we discussed the effects of underlying physical mechanisms on fluid properties relevant to both single-file and collective-diffusion and frictional transport.

ACKNOWLEDGMENTS

The work received support from the Center for Enhanced Nanofluidic Transport (CENT), an Energy Frontier Research Center funded by the U.S. Department of Energy, Office of Science, Basic Energy Sciences under Award No. DE-SC0019112, and the National Science Foundation under Grant No. 2137157. We also acknowledge the Texas Advanced Computing Center (TACC) at The University of Texas at Austin for providing the computing resources on Lonestar6 under Allocation No. DMR22008.

[1] G. H. L. Hagen, Uber die bewegung des wassers in engen cylindrischen rohren, Poggendorf's Ann. Phys. Chem. **46**, 423 (1839).

[2] J. L. M. Poiseuille, *Reserches Experimentales Sur Le Movement Des Liquids Dans Les Tubes De Tres-Petits Diametres* (Imprimerie Royale (Paris), 1844).

[3] R. A. Sampson, On Stokes's current function, Philos. Trans. R. Soc. A **182**, 449 (1891).

[4] Z. Dagan, S. Weinbaum, and R. Pfeffer, An infinite-series solution for the creeping motion through an orifice of finite length, J. Fluid Mech. **115**, 505 (1982).

[5] M. Heiranian, A. Taqieddin, and N. R. Aluru, Revisiting Sampson's theory for hydrodynamic transport in ultrathin nanopores, Phys. Rev. Res. **2**, 043153 (2020).

[6] D. Cohen-Tanugi and J. C. Grossman, Water desalination across nanoporous graphene, Nano Lett. **12**, 3602 (2012).

[7] M. Heiranian, A. B. Farimani, and N. R. Aluru, Water desalination with a single-layer MoS_2 nanopore, Nat. Commun. **6**, 8616 (2015).

[8] J. Feng, M. Graf, K. Liu, D. Ovchinnikov, D. Dumcenco, M. Heiranian, V. Nandigana, N. R. Aluru, A. Kis, and A. Radenovic, Single-layer MoS_2 nanopores at nanopower generators, Nature (London) **536**, 197 (2016).

[9] K. Liu, J. Feng, A. Kis, and A. Radenovic, Atomically thin molybdenum disulfide nanopores with high sensitivity for DNA translocation, ACS Nano **8**, 2504 (2014).

[10] A. B. Farimani, K. Min, and N. R. Aluru, DNA base detection using a single-layer MoS_2, ACS Nano **8**, 7914 (2014).

[11] J. Feng, R. D. Bulushev, S. Khlybov, D. Dumcenco, A. Kis, and A. Radenovic, Identification of single nucleotides in MoS_2 nanopores, Nat. Nanotechnol. **10**, 1070 (2015).

[12] B. F. Farimani, M. Heiranian, M. Kyoungmin, and N. R. Aluru, Antibody subclass detection using graphene nanopores, J. Phys. Chem. Lett. **8**, 1670 (2017).

[13] K. Celebi, J. Buchheim, R. M. Wyss, A. Droudian, P. Gasser, I. Shorubalko, J. I. Kye, C. Lee, and H. G. Park, Ultimate permeation across atomically thin porous graphene, Science **344**, 289 (2014).

[14] S. C. O'Hern, C. A. Stewart, M. S. Boutilier, J. C. Idrobo, S. Bhaviripudi, S. K. Das, J. Kong, T. Laoui, M. Atieh, and R. Karnik, Selective molecular transport through intrinsic defects in a single layer of CVD graphene, ACS Nano **6**, 10130 (2012).

[15] Q. Xie, M. A. Alibakhshi, S. Jiao, Z. Xu, M. Hempel, J. Kong, H. G. Park, and C. Duan, Fast water transport in graphene nanofluidic channels, Nat. Nanotechnol. **13**, 238 (2018).
[16] M. E. Suk and N. R. Aluru, Molecular and continuum hydrodynamics in graphene nanopores, RSC Adv. **3**, 9365 (2013).
[17] J. Buchheim, K. P. Schlichting, R. M. Wyss, and H. G. Park, Assessing the thickness-permeation paradigm in nanoporous membranes, ACS Nano **13**, 134 (2019).
[18] M. E. Suk and N. R. Aluru, Water transport through ultrathin graphene, J. Phys. Chem. Lett. **1**, 1590 (2010).
[19] M. Heiranian and N. R. Aluru, Nanofluidic transport theory with enhancement factors approaching one, ACS Nano **14**, 272 (2020).
[20] S. Gravelle, L. Joly, F. Detcheverry, C. Ybert, C. Cottin-Bizonne, and L. Bocquet, Optimizing water permeability through the hourglass shape of aquaporins, Proc. Natl. Acad. Sci. USA **110**, 41 (2013).
[21] S. Bernèche and B. Roux, Energetics of ion conduction through the K^+ channel, Nature (London) **414**, 73 (2001).
[22] S. Y. Noskov, S. Bernèche, and B. Roux, Control of ion selectivity in potassium channels by electrostatic and dynamic properties of carbonyl ligands, Nature (London) **431**, 830 (2004).
[23] Y. Wang, Z. Cao, and A. B. Farimani, Efficient water desalination with graphene nanopores obtained using artificial intelligence, npj 2D Mater. Appl. **5**, 66 (2021).
[24] J. Eliasson, The rising pressure of global water shortages, Nature (London) **517**, 6 (2015).
[25] M. M. Mekonnen and A. Y. Hoekstra, Four billion people facing severe water scarcity, Sci. Adv. **2**, e1500323 (2016).
[26] J. T. Mueller and S. Gasteyer, The widespread and unjust drinking water and clean water crisis in the United States, Nat. Commun. **12**, 3544 (2021).
[27] M. Elimelech and W. A. Phillip, The future of seawater desalination: Energy, technology, and the environment, Science **333**, 712 (2011).
[28] Q.-L. Zhang, W.-Z. Jiang, J. Liu, R.-D. Miao, and N. Sheng, Water transport through carbon nanotubes with the radial breathing mode, Phys. Rev. Lett. **110**, 254501 (2013).
[29] W. Cao, J. Wang, and M. Ma, Mechano-nanofluidics: Water transport through CNTs by mechanical actuation, Microfluid. Nanofluid. **22**, 125 (2018).
[30] W. Cao, J. Wang, and M. Ma, Carbon nanostructure based mechano-nanofluidics, J. Micromech. Microeng. **28**, 033001 (2018).
[31] J. Wang, W. Cao, M. Ming, and Q. Zheng, Enhanced diffusion on oscillating surfaces through synchronization, Phys. Rev. E **97**, 022141 (2018).
[32] X. Zhou, F. Wu, Y. Liu, J. Kou, H. Lu, and H. Lu, Current inversions induced by resonant coupling to surface waves in a nanosized water pump, Phys. Rev. E **92**, 053017 (2015).
[33] Y. D. Kuang and S. Q. Shi, Strong mechanical coupling between the carbon nanotube and the inner streaming water flow, Microfluid. Nanofluid. **17**, 1053 (2014).
[34] W. H. Duan and Q. Wang, Water transport with a carbon nanotube pump, ACS Nano **4**, 2338 (2010).
[35] Z. Insepov, D. Wolf, and A. Hassanein, Nanopumping using carbon nanotubes, Nano Lett. **6**, 1893 (2006).
[36] S. De and N. R. Aluru, Energy dissipation in fluid coupled nanoresonators: The effect of phonon-fluid coupling, ACS Nano **12**, 368 (2018).
[37] T. Li *et al.*, Control of wettability transition and coalescence dynamics of droplets on the surface via mechanical vibration: A molecular simulation exploration, Appl. Surf. Sci. **473**, 393 (2019).
[38] S. Joseph and N. R. Aluru, Why are carbon nanotubes fast transporters of water? Nano Lett. **8**, 452 (2008).
[39] S. Marbach, N. Kavokine, and L. Bocquet, Resonant osmosis across active switchable membranes, J. Chem. Phys. **152**, 054704 (2020).
[40] S. Marbach and K. Alim, Active control of dispersion within a channel with flow and pulsating walls, Phys. Rev. Fluids **4**, 114202 (2019).
[41] S. Marbach and L. Bocquet, Active sieving across driven nanopores for tunable selectivity, J. Chem. Phys. **147**, 154701 (2017).
[42] R. Sarfati, C. P. Calderon, and D. K. Schwartz, Enhanced diffusive transport in fluctuating porous media, ACS Nano **15**, 7392 (2021).

[43] Y. Noh and N. R. Aluru, Phonon-fluid coupling enhanced water desalination in flexible two-dimensional porous membranes, Nano Lett. **22**, 419 (2022).
[44] Y. Noh and N. R. Aluru, Effect of interfacial vibrational coupling on surface wettability and water transport, Phys. Rev. E **106**, 025106 (2022).
[45] Y. Noh and N. R. Aluru, Ion transport in two-dimensional flexible nanoporous membranes, Nanoscale **15**, 11090 (2023).
[46] N. Li, Z. Feng, H. Lin, J. Zhu, and K. Xu, Accelerating filtration by introducing an oscillation paradigm and its atomistic origin, J. Mater. Chem. A **11**, 297 (2023).
[47] S. Plimpton, Fast parallel algorithms for short-range molecular dynamics, J. Comput. Phys. **117**, 1 (1995).
[48] See Supplemental Material at http://link.aps.org/supplemental/10.1103/PhysRevFluids.9.064201 for a Péclet number analysis of the flow, the pore geometries, the GK cumulative integrals, the classical model fits, and a video of the transient profiles.
[49] G. J. Martyna, M. L. Klein, and M. Tuckerman, Nosé-Hoover chains: The canonical ensemble via continuous dynamics, J. Chem. Phys. **97**, 2635 (1992).
[50] Y. Wu and N. R. Aluru, Graphitic carbon-water nonbonded interaction parameters, J. Phys. Chem. B **117**, 8802 (2013).
[51] R. W. Hockney and J. W. Eastwood, *Computer Simulation Using Particles* (McGraw-Hill, New York, 1981).
[52] H. J. C. Berendsen, J. R. Grigera, and T. P. Straatsma, The missing term in effective pair potentials, J. Phys. Chem. **91**, 6269 (1987).
[53] J.-P. Ryckaert, G. Ciccotti, and H. J. C. Berendsen, Numerical integration of the cartesian equations of motion of a system with constraints: Molecular dynamics of n-alkanes, J. Comput. Phys. **23**, 327 (1977).
[54] C. Huang, K. Nandakumar, P. Y. K. Choi, and L. K. Kostiuk, Molecular dynamics simulation of a pressure-driven liquid transport process in a cylindrical nanopore using two self-adjusting plates, J. Chem. Phys. **124**, 234701 (2006).
[55] J. Li, D. Liao, and S. Yip, Coupling continuum to molecular-dynamics simulation: Reflecting particle method and the field estimator, Phys. Rev. E **57**, 7259 (1998).
[56] B. Corry, Designing carbon nanotube membranes for efficient water desalination, J. Phys. Chem. B **112**, 1427 (2008).
[57] X. Gong, J. Li, H. Lu, R. Wan, J. Li, J. Hu, and H. Fang, A charge driven molecular water pump, Nat. Nanotechnol. **2**, 709 (2007).
[58] J. Li, X. Gong, H. Lu, H. Fang, and R. Zhou, Electrostatic gating of a nanometer water channel, Proc. Natl. Acad. Sci. USA **104**, 3687 (2007).
[59] J. Goldsmith and C. C. Martens, Pressure-induced water flow through model nanopores, Phys. Chem. Chem. Phys. **11**, 528 (2009).
[60] Y. Noh and N. R. Aluru, Activation of atomic transport via vibrational coupling-induced force fluctuations, Appl. Phys. Lett. **123**, 091601 (2023).
[61] G. A. Bird, *The DSMC Method* (CreateSpace Independent Publishing Platform, Scotts Valley, California, 2013).
[62] R. Zwanzig, Diffusion past an entropy barrier, J. Phys. Chem. **96**, 3926 (1992).
[63] R. Zwanzig, Time-correlation functions and transport coefficients in statistical mechanics, Annu. Rev. Phys. Chem. **16**, 67 (1965).
[64] H. Fang, K. Ni, J. Wu, L. Huang, and D. Reible, The effects of hydrogen bonding on the shear viscosity of liquid water, Int. J. Sediment Res. **34**, 8 (2019).
[65] K. Ni, H. Fang, Z. Yu, and Z. Fan, The velocity dependence of viscosity of flowing water, J. Mol. Liq. **278**, 234 (2019).